A Fast Forward Simulation Scheme for Eddy Current Testing of Crack in a Structure of Carbon Fiber Reinforced Polymer Laminate

YALI DU [1,2], **SHEJUAN XIE** [1], **XUDONG LI** [1], **ZHENMAO CHEN** [1],
TETSUYA UCHIMOTO [3], **AND TOSHIYUKI TAKAGI** [3]

[1] State Key Laboratory for Strength and Vibration of Mechanical Structures, Shaanxi Engineering Research Center of Nondestructive Testing and Structural Integrity Evaluation, Xi'an Jiaotong University, Xi'an 710049, China
[2] Department of Applied Physics, School of Science, Xi'an Polytechnic University, Xi'an 710048, China
[3] Institute of Fluid Science, Tohoku University, Sendai 980-8577, Japan

Corresponding authors: Shejuan Xie (xiesj2014@mail.xjtu.edu.cn) and Zhenmao Chen (chenzm@mail.xjtu.edu.cn)

ABSTRACT High frequency Eddy Current Testing (ECT) is one of the key non-destructive testing techniques for ensuring integrity of a structure of Carbon Fiber Reinforced Polymer (CFRP) material. An efficient numerical simulator is indispensable to enhance the performance of quantitative ECT for CFRP structures from both point of view of probe optimization and defect sizing. In this paper, a fast forward simulation scheme based on the A-ϕ formulation and databases approach is proposed, implemented and experimentally validated for the rapid and high precision simulation of ECT signals due to defects in a CFRP plate by updating an FEM-BEM hybrid code for ECT problem. Comparison of numerical results of the present method with those of the conventional full FEM-BEM code and the experimental results for artificial cracks in CFRP laminate plates indicates that the proposed novel fast forward scheme can predict ECT signals over 300 times faster but without worsening numerical accuracy, which enables it to be applied to efficient reconstruction of cracks in CFRP plates and for probe optimization.

INDEX TERMS CFRP, ECT, experimental validation, fast forward numerical scheme, finite element method.

I. INTRODUCTION

In recent decades, carbon fiber reinforced polymer (CFRP) has growing applications in wide engineering fields, e.g., aerospace, transportation, renewable energy etc., due to its light weight and high specific mechanical properties compared with traditional metallic structural materials. However, carbon fiber composite materials have relatively low properties in the direction transverse to their reinforcing fibers, and notably low resistance to impact loads. Impact events are inevitable during the lifetime of a CFRP composite structure during fabrication, service and maintenance due to collisions of small object such as stones or tools. Such events may cause defects of fiber breakage and/or delamination between layers, and severely degrade the loadbearing capacity of the

The associate editor coordinating the review of this manuscript and approving it for publication was Xiaokang Yin.

CFRP structure [1]. A non-destructive testing and evaluation (NDT&E) tool is necessary to detect and evaluate the defects in CFRP laminates during both manufacture and operation processes to ensure the structural integrity.

To date, the most commonly used NDT methods for inspection of CRFP material are ultrasonic testing [2], [3], infrared thermography [4], [5], X-ray [6]–[8] and acoustic emission [9], [10] etc., but all of them have their limitations for NDT of CFRP structure in view of both high accuracy and efficiency. Recently the high frequency eddy current testing (ECT) method is developed for application to inspection and quantitative evaluation of defects in CFRP materials [11]–[20]. In the development of quantitative ECT technique for structure of CFRP materials, a high efficiency numerical code to simulate the ECT signals due to defects in an anisotropic material is of great importance for probe optimization, defect reconstruction and etc. Authors have

developed a finite element and edge element hybrid numerical code based on the reduced vector potential (Ar) formulation for simulation of the ECT of CFRP material [16]. It can give good numerical results but needs large computer resources especially for a CFRP structure of complicated structure and large analysis region. On the other hand, though a fast solver for ECT of isotropic metallic material has already been developed by authors [21]–[29]. The traditional fast solver cannot treat the ECT of anisotropic material such as the CFRP plate, as the conductivity needs to be a constant [30], [31]. In view of these backgrounds, the aim of this paper is to develop a fast forward numerical scheme and solver based on the conventional FEM-BEM hybrid code and the databases type fast forward simulation approach to solve the ECT problem for the anisotropic CFRP material, and to demonstrate its feasibility and efficiency through comparison with both the experimentally measured signals and the numerical results simulated with the conventional full FEM-BEM code. This paper is arranged as follows: First, the anisotropic numerical model and a derivation of the governing formulation for the fast forward scheme based on the FEM-BEM hybrid scheme are presented by taking CFRP plate as example. Second, the fast forward scheme is implemented in our FEM-BEM hybrid code for ECT of the CFRP material and the pick-up signals due to a crack in the inspection target are calculated for comparison with those obtained with the conventional full FEM-BEM code. At last, an experimental system and ECT signals of artificial cracks in a CFRP plate are established and measured to further experimentally prove the validity of the fast forward solver for ECT of anisotropic material. The concluding remarks are given at last part.
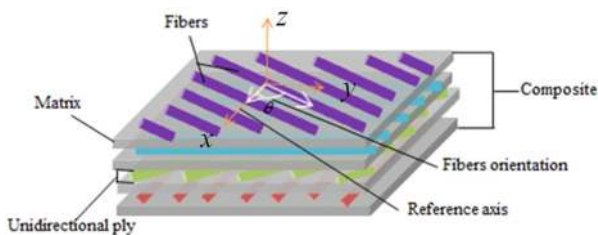

FIGURE 1. Structure of the considered CFRP plate.

II. FAST FORWARD SCHEME FOR ECT OF CRFP MATERIAL
A. NUMERICAL MODEL FOR ECT OF CFRP PLATE
The typical structure of the CFRP material to be considered is illustrated in Fig.1. The CFRP plate is made by stacking several unidirectional plies of different fibers orientation. Each unidirectional ply is constituted of carbon fibers embedded in an electrical nonconductive matrix. The conductivity in the direction transverse to the fiber orientation is not full nil because there are contacts between carbon fibers which are not perfectly aligned and covered by matrix material.

When the plies of CFRP are assembled, there are also some contacts between the fibers of the adjacent plies, i.e., it is also

partly conductive between plies but the conductivity is also relative small. Though the CFRP material is not uniform from micro-point of view, it can be treated as a homogenous material in ECT simulation as the fiber diameter is much smaller than the size of the ECT probe. However, the conductivity of the CFRP material has to be expressed in form of a tensor as shown in (1) as it depends on the direction the carbon fibers. The conductivity tensor of each ply depends on the type, the volume fraction and the orientation of the fibers in the plies. In (1), σ_L and σ_T are the longitudinal and transversal conductivity in the plies, θ is the orientation angle of the fibers in the ply, and σ_{CP} is the cross ply conductivity.

$$\bar{\bar{\sigma}} = \begin{bmatrix} \sigma_L \cos^2\theta + \sigma_T \sin^2\theta & \dfrac{\sigma_L - \sigma_T}{2}\sin 2\theta & 0 \\ \dfrac{\sigma_L - \sigma_T}{2}\sin 2\theta & \sigma_L \sin^2\theta + \sigma_T \cos^2\theta & 0 \\ 0 & 0 & \sigma_{cp} \end{bmatrix}$$
(1)

The longitudinal conductivity σ_L is related with the conductivity of the carbon fiber σ_f, the conductivity of the matrix σ_m and the fiber volume fraction V_f [32] in form of.

$$\sigma_L = \sigma_f V_f + \sigma_m(1 - V_f)$$
(2)

However, the transverse conductivity σ_T and the through-thickness conductivity σ_{CP} depend on the average waviness of the fibers. As the fibers in plies are not fully straight and parallel each other but twisted a little, the fibers may contact each other. If the volume fraction of fibers increases, more fiber contacts occur. It has already been reported that the resistance of fibers and fiber-contact-network cause nonzero electrical conductivity of a CFRP composite [32], [33]. Therefore, the transverse conductivity and the through-thickness conductivity are usually varied due to different manufacturing and processing method and processes.
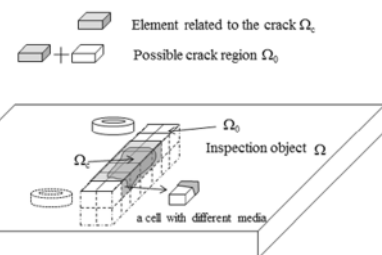

FIGURE 2. Numerical model for fast simulation of ECT signals.

Figure 2 gives a numerical model of ECT inspection for the CFRP laminates plate, which is similar to the model utilized for ECT of metallic material given in paper [21]. A self-induction pancake coil and a surface breaking crack with complex shape are shown as example of ECT probe and defect. In Fig.2, Ω denotes the whole unflawed inspection object, Ω_c is the crack region and Ω_0 is a selected regular shaped region containing the crack. The governing equation of the anisotropic ECT problem based on the $A - \phi$

formulation is as those shown in the following low frequency Maxwell equations with the displacement current term neglected.

$$\frac{1}{\mu_0}\nabla^2 A - \bar{\bar{\sigma}}(r)(A + \nabla\phi) = 0 \qquad (3)$$

$$\nabla \cdot \bar{\bar{\sigma}}(r)(A + \nabla\phi) = 0 \qquad (4)$$

in CFRP material. In air region around the CFRP material, the governing equation is

$$\frac{1}{\mu_0}\nabla^2 A = -J_0 \qquad (5)$$

where A and ϕ are respectively the magnetic vector potential and electric scalar potential for the CFRP object with flaw present, J_0 is the current density in the region of ECT excitation coil, $\bar{\bar{\sigma}}_0$ is the conductivity tensor of the unflawed host CFRP conductor, $\bar{\bar{\sigma}}(r)$ is the conductivity tensor at point r in the CFRP with flaw, which is 0.0 in the crack region and $\bar{\bar{\sigma}}_0$ in the base material zone, μ_0 is the permeability of the host conductor and the air, i.e., the CFRP is considered as a nonmagnetic material.

To solve the above governing equations with the FEM-BEM hybrid code [29], the full inspection target and the crack region are meshed into FEM elements, while the influence of the coils is considered with the BEM, which enables easy simulation of ECT coils at different scanning location. However, to apply the full FEM-BEM code for crack reconstruction from ECT signals, huge simulation burden is necessary as a lot of 3-D FEM-BEM problems have to be solved during the inversion procedure and a new mesh has to be subdivided for each iteration as the crack profile is different.

To enhance the simulation efficiency for inversion of crack in an isotropic metallic material, authors have developed a database type fast forward solver [21]–[29] for efficient simulation ECT signal. The key of the method is to localize the simulation area to the crack region by using the databases of unflawed potential information pre-calculated and stored for a given defect suspicious region Ω_0. By using the fast numerical scheme, the ECT signals due to any crack making up by the cells subdividing the region Ω_0 (see Fig.2 as example) can be efficiently calculated as the region of crack is usually very small compared with the total inspection target. The details of the database type fast numerical scheme can be found in paper [21]. However, this fast numerical scheme cannot be directly applied to the ECT problem of the CFRP materials due to the anisotropic material property. In the following subsections, an upgrade to the fast numerical simulation scheme is proposed for ECT of the anisotropic CFRP materials with detailed numerical formulation and practical implementation.

B. THEORY OF THE FAST FORWARD SCHEME FOR ECT OF ANISOTROPIC MATERIAL

Referring to (3) to (5), the governing equations for ECT of an unflawed CFRP material become (6) and (7) in material region and (8) in air region, i.e.,

$$\frac{1}{\mu_0}\nabla^2 A^u - \bar{\bar{\sigma}}_0(A^u + \nabla\phi^u) = 0 \qquad (6)$$

$$\nabla \cdot \bar{\bar{\sigma}}_0(A^u + \nabla\phi^u) = 0 \qquad (7)$$

$$\frac{1}{\mu_0}\nabla^2 A^u = -J_0 \qquad (8)$$

where A^u and ϕ^u are respectively the magnetic vector potential and electric scalar potential of the unflawed CFRP object. Subtracting (6) - (8) from (3) - (5), one can find

$$\frac{1}{\mu_0}\nabla^2 A^f - \bar{\bar{\sigma}}_0(A^f + \nabla\phi^f) = -\left[\bar{\bar{\sigma}}_0 - \bar{\bar{\sigma}}(r)\right](A + \nabla\phi) \quad (9)$$

$$\nabla \cdot \bar{\bar{\sigma}}_0(A^f + \nabla\phi^f) = \nabla \cdot \left[\bar{\bar{\sigma}}_0 - \bar{\bar{\sigma}}(r)\right](A + \nabla\phi)$$
$$\text{(in conductor)} \qquad (10)$$

$$\frac{1}{\mu_0}\nabla^2 A^f = 0 \quad \text{(in air)} \qquad (11)$$

where, A^f and ϕ^f are the perturbations of magnetic vector potential and electric scalar potential due to the presence of a crack, i.e., $A^f = A - A^u$, $\phi^f = \phi - \phi^u$. Comparing (9)-(11) with (6)-(8), one can find that the only difference is the terms with the coefficient $\bar{\bar{\sigma}}_0 - \bar{\bar{\sigma}}(r)$. This means that the left hand of the two sets of system equations will be the same after being discretized with the FEM-BEM hybrid method, i.e., the presence of a crack only affects the term related to $\bar{\bar{\sigma}}_0 - \bar{\bar{\sigma}}(r)$.

Meshing region $\Omega - \Omega_c$ with normal finite element and the Ω_c region with the cells subdividing Ω_c region as given in Fig. 2, Eq. (9), (10) and (11) can be discretized to the system of linear equations of the FEM-BEM hybrid method as follows if the crack region Ω_c is exactly made up by the cells subdivided previously,

$$[P + K + j\omega Q + j\omega R]\begin{Bmatrix} A^f \\ \Phi^f \end{Bmatrix} = \left[j\omega Q' + j\omega R'\right]\begin{Bmatrix} A \\ \Phi \end{Bmatrix} \quad (12)$$

where, $[P]$ is the coefficient matrix derived from the first term in the left hand of (9), $[Q]$ the coefficient matrix corresponding to the second term of (9), $[R]$ the coefficient matrix of (10) discretized with FEM and $[K]$ is the coefficient matrix of (10) discretized with BEM [21]. Only matrices $[Q]$ and $[R]$ are related to the anisotropic conductivity tensor, and $[Q']$ and $[R']$ have similar form with matrices $[Q]$ and $[R]$. The details of the element coefficient matrix $[Q + R]$ and $[Q' + R']$ are in form of (13).

$$[Q + R] = \begin{bmatrix} N_{2a} & N_a & 0 & N_{3a} \\ N_b & N_{2b} & 0 & N_{3b} \\ 0 & 0 & N_{2c} & N_{3c} \\ N_{3a}^T & N_{3b}^T & N_{3c}^T & N_d \end{bmatrix}$$

$$[Q' + R'] = \begin{bmatrix} N_{2a}' & N_a' & 0 & N_{3a}' \\ N_b' & N_{2b}' & 0 & N_{3b}' \\ 0 & 0 & N_{2c}' & N_{3c}' \\ N_{3a'}^T & N_{3b'}^T & N_{3c'}^T & N_d' \end{bmatrix} \quad (13)$$

where the submatrices have the following expressions,

$$[N_{2a}] = \left(\sigma_{0L}\cos^2\theta + \sigma_{0T}\sin^2\theta\right)\int_{\Omega_e}[N]^T[N]dv \quad (14)$$

$$[N_{2b}] = \left(\sigma_{0L}\sin^2\theta + \sigma_{0T}\cos^2\theta\right)\int_{\Omega_e}[N]^T[N]dv \quad (15)$$

$$[N_{2c}] = \sigma_{0cp}\int_{\Omega_e}[N]^T[N]dv \quad (16)$$

$$[N_a] = 0.5(\sigma_{0L} - \sigma_{0T})\sin 2\theta\int_{\Omega_e}[N]^T[N]dv \quad (17)$$

$$[N_b] = 0.5(\sigma_{0L} - \sigma_{0T})\cos 2\theta\int_{\Omega_e}[N]^T[N]dv \quad (18)$$

$$[N_{3a}] = (\sigma_{0L}\cos^2\theta + \sigma_{0T}\sin^2\theta)\int_{\Omega_e}[N]^T\left[\frac{\partial N}{\partial x}\right]dv$$
$$+ 0.5(\sigma_{0L} - \sigma_{0T})\sin 2\theta\int_{\Omega_e}[N]^T\left[\frac{\partial N}{\partial y}\right]dv \quad (19)$$

$$[N_{3b}] = 0.5(\sigma_{0L} - \sigma_{0T})\sin 2\theta\int_{\Omega_e}[N]^T\left[\frac{\partial N}{\partial x}\right]dv$$
$$+ (\sigma_{0L}\sin^2\theta + \sigma_{0T}\cos^2\theta)\int_{\Omega_e}[N]^T\left[\frac{\partial N}{\partial y}\right]dv \quad (20)$$

$$[N_{3c}] = \sigma_{0cp}\int_{\Omega_e}[N]^T\left[\frac{\partial N}{\partial z}\right]dv \quad (21)$$

$$[N'_{2a}] = ((\sigma_{0L} - \sigma_L(\boldsymbol{r}))\cos^2\theta$$
$$+ (\sigma_{0T} - \sigma_T(\boldsymbol{r}))\sin^2\theta)\int_{\Omega_e}[N]^T[N]dv \quad (22)$$

$$[N'_{2b}] = ((\sigma_{0L} - \sigma_L(\boldsymbol{r}))\sin^2\theta$$
$$+ (\sigma_{0T} - \sigma_T(\boldsymbol{r}))\cos^2\theta)\int_{\Omega_e}[N]^T[N]dv \quad (23)$$

$$[N'_{2c}] = (\sigma_{0cp} - \sigma_{cp}(\boldsymbol{r}))\int_{\Omega_e}[N]^T[N]dv \quad (24)$$

$$[N'_a] = 0.5(\sigma_{0L} - \sigma_L(\boldsymbol{r}) - \sigma_{0T}$$
$$+ \sigma_T(\boldsymbol{r}))\sin 2\theta\int_{\Omega_e}[N]^T[N]dv \quad (25)$$

$$[N'_b] = 0.5(\sigma_{0L} - \sigma_L(\boldsymbol{r}) - \sigma_{0T}$$
$$+ \sigma_T(\boldsymbol{r}))\sin 2\theta\int_{\Omega_e}[N]^T[N]dv \quad (26)$$

$$[N_{3a}] = ((\sigma_{0L} - \sigma_L(\boldsymbol{r}))\cos^2\theta + (\sigma_{0T} - \sigma_T(\boldsymbol{r}))\sin^2\theta)$$
$$\times\int_{\Omega_e}[N]^T\left[\frac{\partial N}{\partial x}\right]dv + 0.5(\sigma_{0L} - \sigma_L(\boldsymbol{r}) - \sigma_{0T}$$
$$+ \sigma_T(\boldsymbol{r}))\sin 2\theta\int_{\Omega_e}[N]^T\left[\frac{\partial N}{\partial y}\right]dv \quad (27)$$

$$[N_{3b}] = 0.5(\sigma_{0L} - \sigma_L(\boldsymbol{r}) - \sigma_{0T} + \sigma_T(\boldsymbol{r}))\sin 2\theta$$
$$\times\int_{\Omega_e}[N]^T\left[\frac{\partial N}{\partial x}\right]dv + ((\sigma_{0L} - \sigma_L(\boldsymbol{r}))\sin^2\theta$$
$$+ (\sigma_{0T} - \sigma_T(\boldsymbol{r}))\cos^2\theta)\int_{\Omega_e}[N]^T\left[\frac{\partial N}{\partial x}\right]dv \quad (28)$$

$$[N_{3c}] = (\sigma_{0cp} - \sigma_{cp}(\boldsymbol{r}))\int_{\Omega_e}[N]^T\left[\frac{\partial N}{\partial z}\right]dv \quad (29)$$

$$\left[N_d^{ij}\right] = \left[\int_{\Omega_e}\nabla N^i\cdot(\bar{\bar{\sigma}}_0 - \bar{\bar{\sigma}}(\boldsymbol{r}))\nabla N^j dv\right] \quad (30)$$

$$\left[N_d'^{ij}\right] = \left[\int_{\Omega_e}\nabla N^i\cdot\bar{\bar{\sigma}}_0\nabla N^j dv\right] \quad (31)$$

where Ω_e is the volume of the finite element under consideration. $[N]$ is a line matrix of shape functions at the coordinate vector $\boldsymbol{r}$ which interpolates the unknown field values by

$$\boldsymbol{A}(\boldsymbol{r}) = [N(\boldsymbol{r})]\{A\}$$
$$\phi(\boldsymbol{r}) = [N(\boldsymbol{r})]\{\phi\} \quad (32)$$

As the conductivity are included in all the formulae for element coefficient matrices, i.e., Eq.(14)-(31), the element coefficient matrices in right hand of Eq.(33) become zero for the unflawed elements as $\bar{\bar{\sigma}}_0 - \bar{\bar{\sigma}}(\mathrm{r}) = 0$ for these elements. Thus, (12) can be expressed as the following submatrix form

$$\begin{bmatrix}\overline{K}_{11} & \overline{K}_{12}\\\overline{K}_{21} & \overline{K}_{22}\end{bmatrix}\begin{Bmatrix}q_1^f\\q_2^f\end{Bmatrix} = \begin{bmatrix}\widetilde{K}_{11} & 0\\0 & 0\end{bmatrix}\begin{Bmatrix}q_1^f + q_1^u\\q_2^f + q_2^u\end{Bmatrix} \quad (33)$$

where $[\bar{K}] = [P] + [K] + j\omega[Q + R]$, $[\tilde{K}] = j\omega\left[Q' + R'\right]$, $\{q^f\} = \{A^f, \phi^f\}$ and $\{q^u\} = \{A^u, \phi^u\}$. In (33), the potential vector $\{q\}$ is divided into two parts: $\{q_1\}$ are the potentials at nodes of crack elements, $\{q_2\}$ are the potentials at other nodes, and the superscript f and u denote the field perturbation due to flaw and the unflawed field. Multiplying (33) with $[H] = \left[\bar{K}\right]^{-1}$, we get

$$\begin{Bmatrix}q_1^f\\q_2^f\end{Bmatrix} = \begin{bmatrix}H_{11} & H_{12}\\H_{21} & H_{22}\end{bmatrix}\begin{bmatrix}\widetilde{K}_{11} & 0\\0 & 0\end{bmatrix}\begin{Bmatrix}q_1^f + q_1^u\\q_2^f + q_2^u\end{Bmatrix} \quad (34)$$

Denoting $[G] = [H_{11}][\tilde{K}_{11}]$ and the unit matrix as $[I]$, the relation between the field perturbation $\{q_1^f\}$ and the unflawed field $\{q_1^u\}$ can be finally derived as

$$[I - G]\left\{q_1^f\right\} = [G]\left\{q_1^u\right\} \quad (35)$$

The solution of the perturbed field $\{q_1^f\}$ using system of linear equation (35) is much faster than to solve the conventional full FEM–BEM equations, because the unknowns of (35) are limited to the elements related to crack region Ω_c. The coefficient matrices $[H_{11}]$ and $\{q_1^u\}$ containing the information of the CFRP material and the exciting coils can be calculated *a priori* as they are independent of the crack for a given inspection CFRP target plate. Thus, once these unflawed fields have been re-calculated and stored as databases, one does not need to compute them again for calculating perturbed ECT signals due to a crack of different profile. Consequently, the computational burden can be significantly reduced for the forward analysis but without worsen the numerical precision.

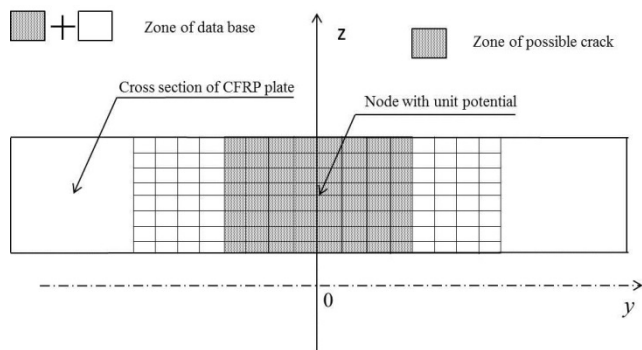### C. ESTABLISHMENT OF THE DATABASES OF UNFLAWED POTENTIAL INFORMATION

For the scheme described in the previous subsection, to establish the databases for $[H_{11}]$ and $\{q_1^u\}$ are very important. Therefore, the crack suspicious region Ω_0 and its mesh grid have to be properly chosen in order to establish the unflawed potential databases. Usually, the region Ω_0 can be selected based on the information of the measured ECT signals in case to reconstruct the profile of a crack in a CFRP plate.

In practice, the possible position and the size of a crack can be roughly determined based on the position of the signal peak and the area of relative large ECT signal. The width of the crack, on the other hand, can be set as a small constant value (e.g., 0.2 mm) as it does not influence the ECT signals significantly for a fatigue crack and also can be covered through a calibration on the measured signals. Consequently, we can choose a thin regular shaped planar zone including the possible crack region as the crack suspicious region Ω_0. By subdividing the planar region Ω_0 into a regular mesh of small elements, the unflawed field $\{q_1^u\}$ at the nodes of these cells, and the sub-inverse matrix $[H_{11}]$ can be obtained by using the full FEM–BEM code. In practice, the submatrix $[H_{11}]$ of the inverse matrix of $[K]$ can be calculated by solving the following system of equations

$$[K]\{q\} = \{\delta_{ij}\}, \quad i = 1, 2, \ldots, n; \ j = 1, 2, 3, 4 \quad (36)$$

where, n is the total number of nodes related to the region Ω_0 and δ_{ij} is a unit vector of $4n$ elements whose only nonzero element $(=1.0)$ corresponds to the i-th node and j-th potential component. Equation (36) is equivalent to putting a harmonic unit potential of j-th component at the i-th node of the unflawed conductor. The solution vector of (36) is a column of the inverse matrix $[H]$ with a column number determined by the node number and the potential component. Once the potentials induced by a unit potential acting at every node in Ω_0 are pre-calculated and stored in a database *a priori* (Fig. 3), the inverse matrix $[H_{11}]$ of an arbitrary crack in Ω_0 can be extracted from the information stored in database directly by selecting proper data columns.

FIGURE 3. The region where a priori knowledge of unflawed potential has to be pre-calculated and stored.

When considering an ECT problem of large multi-layered CFRP plate, the establishment of databases can be simplified in case that the anisotropic conductivity is uniform in each layer. The eddy currents fields are of the same value and distribution for the same excitation source at different position at a given layer if the target plate is infinite large though the distribution is shifted according to the position of excitation coil. In practice, if the CFRP plate is large enough compared with the probe, such a shifting property is also valid approximately even for the anisotropic and equivalently

homogenous CFRP plate. Therefore, we only need to calculate the unflawed potential fields when the unit sources are located at the nodes of the center of the different plate layers. The unflawed potential field due to a source at other position other than the center point can be obtained by simply shifting the results due to the same source but at the center of same plate layer. In other words, the field $E(x, y, z; x_s, y_s, z_s)$ excited at the position (x_s, y_s, z_s) connects with the field $E(x, y, z; 0, 0, z_s)$ excited at the center point $(0, 0, z_s)$ of the same layer according the shifting correlation

$$E(x, y, z; x_s, y_s, z_s) = E(x - x_s, y - y_s, z; 0., 0., z_s) \quad (37)$$

Using (37), only the fields due to a source located at the center of the fiber layers of the CFRP plate need to be pre-calculated and stored in the databases. The others required in $[H_{11}]$ can be obtained from the unflawed potentials of the central source by simply shifting the x and y coordinate based on (37). In practice, the unflawed potentials at a wider range than Ω_0 have to be calculated and stored in the databases in order to use the shifting strategy.

As for the database of $\{q_1^u\}$, similar approach can be adopted. In practice, only the unflawed potential field due to coil at the center of the plate of given liftoff, orientation and testing conditions has to be pre-calculated by using the full FEM-BEM code. The $\{q_1^u\}$ due to the coil at other scanning points can be obtained from the field excited by the coil at the center by just shifting their coordinates. In this way, significant computer resources needed for the forward simulations using the full FEM-BEM can be reduced in order to establish the unflawed databases.

D. IMPEDANCE SIGNAL CALCULATION

As the fast forward solver only can give eddy current field perturbation in the flaw region, the conventional way using the Faraday and the Biot-Savart's Law is not suitable for the pick-up impedance signal calculation. Fortunately, same as the case of the isotropic metallic material, the impedance change of a self-induction pancake coil can be calculated as follows based the reciprocal theorem

$$\Delta Z = \frac{1}{I^2} \int_{flaw} E_e^u \cdot (\bar{\bar{\sigma}}_0 - \bar{\bar{\sigma}}(r))(E_e^f + E_e^u)dv \quad (38)$$

where ΔZ is the impedance change in the self-induction coil due to the presence of a crack, E_e^u and E_e^f are respectively the unflawed field and its perturbation induced by the excitation coil, and $(\bar{\bar{\sigma}}_0 - \bar{\bar{\sigma}}(r))(E_e^f + E_e^u)$ is the eddy current in the flaw region. Equation (38) can be efficiently integrated by using the element coefficient matrices which have already been formed during the FEM-BEM discretization in the new fast forward scheme.

III. IMPLEMENTATION AND NUMERICAL VALIDATION
Based on the formulae and numerical scheme given in the section II, a fast forward solver for simulation of ECT of the CFRP problem is developed. To demonstrate its validity and the efficiency, ECT signals of a pancake coil over an artificial

TABLE 1. Parameters of CFRP plate and crack models.

Plate models (A/B/C/D)	Length(mm)		40
	Width(mm)		40
	Thickness(mm)		1
	Stacking sequence	A	$[0_2^0, 0_2^0, 0_2^0, 0_2^0]$
		B	$[0_2^0, 90_2^0, 0_2^0, 90_2^0]$
		C	$[0_2^0, 45_2^0, 0_2^0, 45_2^0]$
		D	$[0_2^0, 45_2^0, 90_2^0, 145_2^0]$
	Conductivity		(1000,100,100)
Crack (A/B/C/D)	Length(mm)		4.0
	Width(mm)		0.2
	Depth(mm)		0.75

slit in a CFRP plate were simulated by using both the new fast forward solver and the full FEM-BEM code developed for anisotropic material [16] and compared for validation.

A. NUMERICAL MODEL AND ESTABLISHMENT OF DATABASES

4 kinds of CFRP laminate plates of different fiber orientations are simulated by using the new fast solver and the conventional full FEM-BEM code. Table 1 gives the parameters of the inspection target CFRP plate of different fiber orientation and the cracks to be detected. The stacking sequence represents the angle between the fiber and the *x* axis. Every four layers the stacking sequence is repeated, i.e., the subscript 2 denotes two stacking sequence. The plates are 40 mm in length (*x* direction), 40 mm in width (*y* direction) and 1 mm in thickness (*z* direction) respectively, and are subdivided into 17 elements in *x* direction, 28 elements in *y* direction, 8 elements in *z* direction for the full FEM-BEM simulation and the fast FEM-BEM method. As the numbers of CFRP layers and the element layer are the same, all the finite elements have uniform anisotropic conductivity though they are different for different layers.
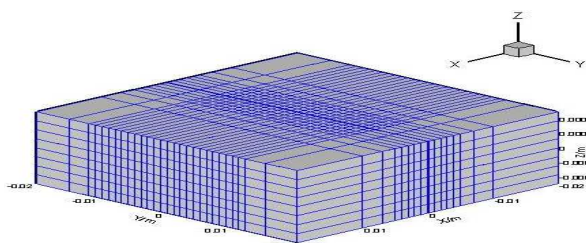
FIGURE 4. The mesh divisions of the numerical models.

The surface crack to be inspected is set at the center of the CFRP plate along *y* direction and its size are selected as 4.0 mm (4 elements) in length, 0.2 mm (1 element, in *x* direction) in width and 0.75 mm (6 elements, *z* direction) in depth. Fig.4 shows the mesh division of the plate model, where finer meshes are used for the crack region. The electric conductivity in the longitudinal, transversal and cross-ply directions are set as 10000 S/m, 100 S/m and 100 S/m

respectively [34]. The ECT probe is selected as a pancake coil and the scanning direction is along the length direction of the crack (*y* direction). The liftoff is chosen as 1.0 mm and the excitation frequency is chosen as 1 MHz.

According to what stated in the section II.C, a 0.2 mm thickness planar region of dimensions 8 mm × 1 mm in the *y-z plane* was chosen as the crack suspicious region Ω_0 and was subdivided into 8 × 8 cubic elements. Both vector and scalar potentials at a region twice as long as the region Ω_0 in *y* direction due to unit potentials at plate center were calculated and stored in the database for the inverse matrix $[H_{11}]$, while the unflawed potential values due to the excitation coil at a region with 24 mm (−12, 12mm) length were calculated and stored for the database of unflawed field $\{q_1^u\}$ to cope with the 16 mm scanning range based on the shifting algorithm.

B. NUMERICAL RESULTS

Figure 5 shows the real and imaginary ECT signals at 17 scanning points (from -8 mm to 8 mm with an interval of 1 mm and along crack length direction) simulated with the full FEM-BEM code and the new database type fast solver for the anisotropic material and testing conditions shown in Table. 2.

TABLE 2. Parameters of ECT coil and test conditions.

Coil	Inner diameter(mm)	1.2
	Outer diameter (mm)	3.2
	Height (mm)	0.8
	Number of turns	140
Test condition	Exciting current(A)	1.0
	Lift-off(mm)	1.0
	Frequency(MHz)	1.0

**TABLE 3.** Comparison between fast solver and full FEM-BEM method for four.

	Time of Full FEM-BEM (s)	Time of Fast solver (s)	Error
Crack A	1642.02	4.24	2.45%
Crack B	1972.89	5.83	3.63%
Crack C	2264.23	6.26	2.28%
Crack D	2557.00	6.49	3.84%

The detailed simulation time and errors are given in Table 3 with the "Error" defined by

$$Error = Max \left| \frac{Z_{fast}(n) - Z_{full-FEM-BEM}(n)}{Z_{full-FEM-BEM}(n)} \right| \times 100\% \quad (39)$$

where *n* represents the *n*-th scanning point, $Z_{fast}(n)$ denotes the impedance at the *n*-th scanning point calculated using the database type fast ECT solver, and $Z_{full\ FEM-BEM}(n)$ denotes the impedance signal calculated using the full FEM-BEM method. Both the results of the fast solver and the full FEM-BEM code are obtained under the same computation conditions.

Although the two results are in very good agreement as shown in Fig.5, the full FEM-BEM method took about half

(a)

(b)

(c)

(d)
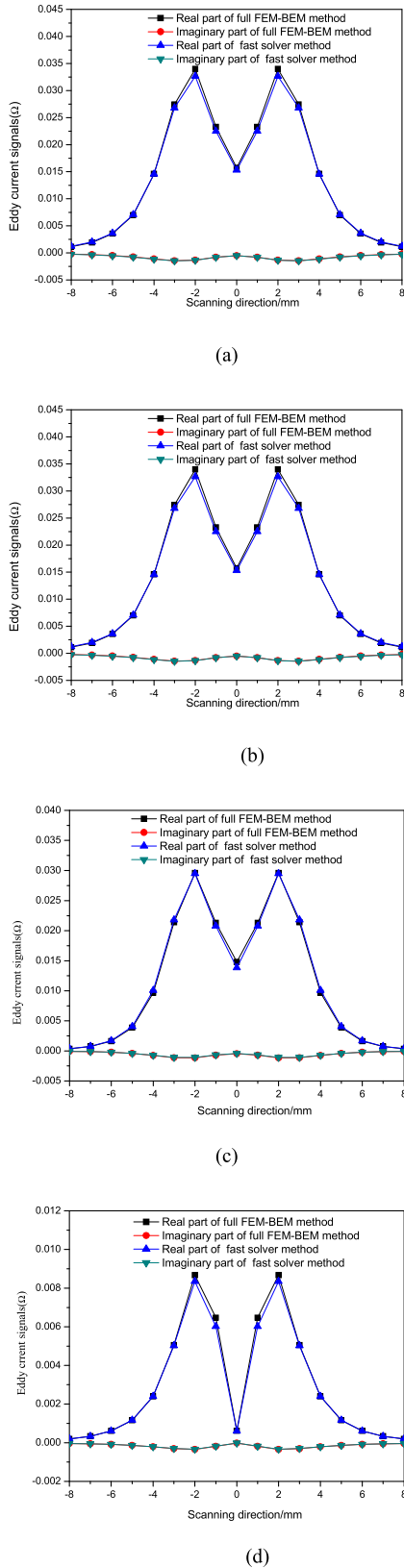
FIGURE 5. Comparison results of fast solver and full FEM-BEM. (a) model A: $[0^0_2, 0^0_2, 0^0_2, 0^0_2]$, (b) model B: $[0^0_2, 90^0_2, 0^0_2, 90^0_2]$, (c) model C: $[0^0_2, 45^0_2, 0^0_2, 45^0_2]$, (d) model D: $[0^0_2, 45^0_2, 90^0_2, 135^0_2]$.

hour to obtain the results while the fast solver only need about 5 seconds, i.e., the fast solver is more than 300 times faster as shown in Table 3. At the same time, the errors between the developed and full FEM-BEM solvers are around 3%. They mainly come from the shifting symmetric strategy due to the boundary effect and the numerical integration for signal calculation. By enlarging the geometry for database establishment and to use more Gauss integration points, the errors can be reduced. The closely matched numerical results and the greatly reduced CPU time confirm the validity and efficiency of the proposed fast scheme and code for simulating ECT problem of the anisotropic material.

With regard to the database, it took about half hour to build for the both the unflawed fields due to the coil and the unit potential sources. Once the database is well established, each forward analysis only takes a few seconds. Though the establishment of databases takes time, it is not a big problem for application to crack reconstruction as a large number of forward simulations have to be conducted for the inverse analysis, but the databases only need to be established once before the inverse analysis.

IV. VALIDATIONS BASED ON EXPERIMENTS
A. CONDUCTIVITY MEASUREMENT OF CFRP PLATES

To validate the fast forward simulation code for ECT of the practical CFRP plate, the electric conductivity of the target CFRP plate in three directions are measured. Three specimens of dimensions 100 mm in both the length and width, 3 mm in thickness are fabricated with use of a CFRP plate of 12 unidirectional plies of ply thickness 0.25 mm. The four electrodes potential drop method was adopted to measure the conductivity in 3 directions respectively. The configuration of electrodes arrangements is shown in Fig.6 [35]. As the characterization of conductivity with regard to frequency is based on an impedance measurement, consisting in injecting an alternating current with an AC power source. The roles of the Volt meter and the Ampere meter in Fig. 6 are to calculate the impedance, Z = U/I. The setup shown in Fig.6 (a) is used to measure the longitudinal conductivity by driving current along the fibers direction, while setup Fig.6 (b) and (c) are used to measure the transversal conductivity and the through-thickness conductivity. The edge of the CRFP samples were carefully polished to expose the fibers and painted with silver paste to make the electrodes well contact with the CFRP plate.

The electric properties of the samples in the three directions are measured by using a LCR tester. The resistivity along the fiber is 0.901 mΩ.m, transverse to the fiber is 0.223 mΩ.m and through the thickness is 27.8 mΩ.m at 3 MHz. By using the correlation of the conductivity and the total resistances based on an assumption that the current in all samples are uniform. The conductivity σ_L, σ_T and σ_{CP} of the CFRP plate are obtained as (1110, 4.48, 0.036) S/m at 3 MHz.
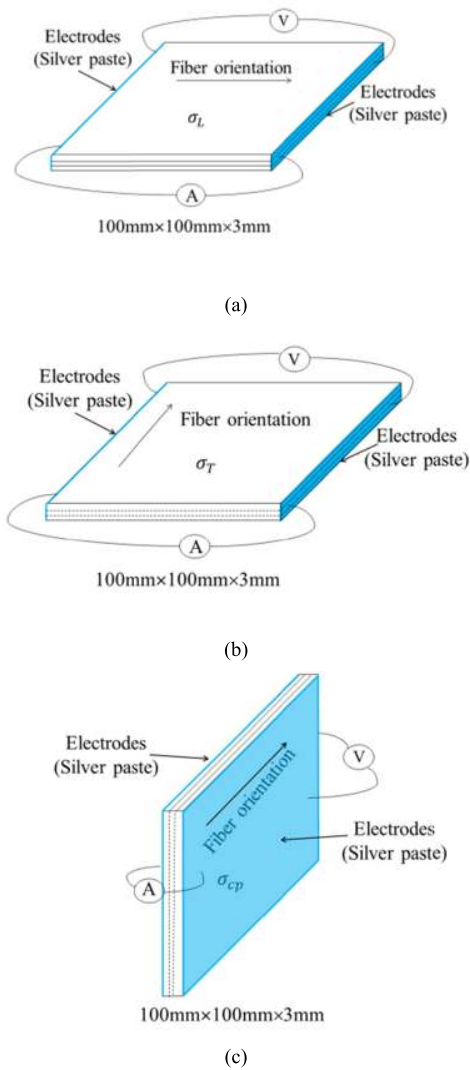
(a)

(b)

(c)

FIGURE 6. The configuration of electrodes on the specimens. (a) Longitudinal. (b) Transversal. (c) Through-thickness.
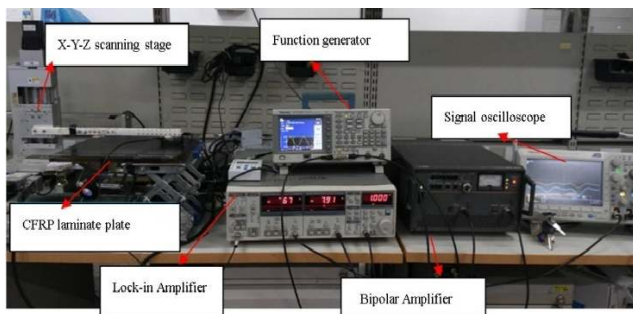

FIGURE 7. Experimental system of ECT inspection for CFRP plate.

B. ECT EXPERIMENTS FOR THE CFRP PLATE

To experimental validation of the new fast forward simulation scheme, an ECT experimental system is established as shown in Fig.7. The system mainly consists of a signal generator,
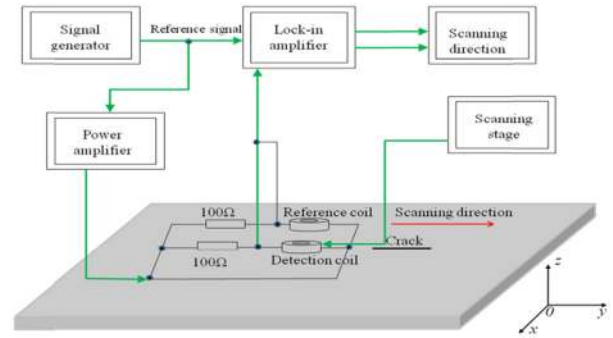

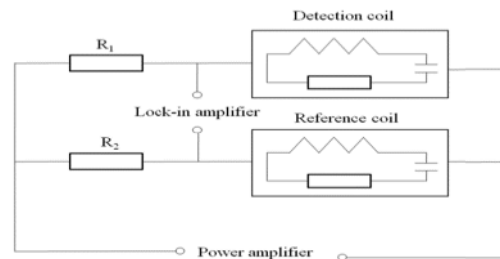**FIGURE 8.** Experimental system of ECT inspection for CFRP plate.

FIGURE 9. AC electric bridge for ECT measurement.

a lock-in amplifier, a digital oscilloscope and an automatic 2D scanning stage. The configurations of the specimen and the ECT probe are shown in Fig.8. The Vx and Vy output of the lock-in amplifier are connected to the CH1 and CH2 channel of the oscilloscope. To enhance the sensitivity, a reference coil is adopted at a given position far from the crack, and is connected with the detection coil through an electric bridge as shown in Fig.9. The reference coil is just the same with the detection coil in both shape and size. In the electric bridge, both the resistance R_1 and R_2 are chosen as 100 Ω, which is about the same value with the coil impedance. The detection coil is scanned over the CFRP test-piece plate along the artificial slit by the automatic 2D scanner. Two test-pieces are fabricated with a CFRP plate of 12 unidirectional plies of 0.25 mm thickness each, and a rectangular slit was fabricated in the center of the test-piece to simulate fiber brakeage. The detailed parameters of the test-piece are listed in Table 4. The test samples are subdivided into 9 elements in x direction, 20 elements in y direction, 12 elements in z direction for the full FEM-BEM simulation and the fast solver. Meanwhile the crack C1 and C2 were divided into $1 \times 6 \times 10$ and $1 \times 6 \times 8$ elements in width, length and depth respectively. According to what stated in the section II.C, a 1.6mm (2.0mm) thickness planar region of dimensions 40mm $\times$ 3mm in the y-z plane was chosen as the crack suspicious region Ω_0 and was subdivided into 16×12 cubic elements. A hand-make pancake coil probe with the dimension and the testing conditions given in Table 5 are adopted to detect the slit in the CFRP laminate

TABLE 4. Parameters of CFRP plate sample and cracks.

Plate models	Length(mm)	80
	Width(mm)	40
	Thickness(mm)	3
	Stacking sequence	$[45_3^0, 90_3^0, 135_3^0, 0_3^0]$
	Conductivity(S/m)	(1110, 4.48, 0.036)
Crack	Length(mm)	20
C1/C2	Width(mm)	1.6/2.0
	Depth(mm)	2.0/1.5

TABLE 5. Parameters of ECT coil and test conditions.

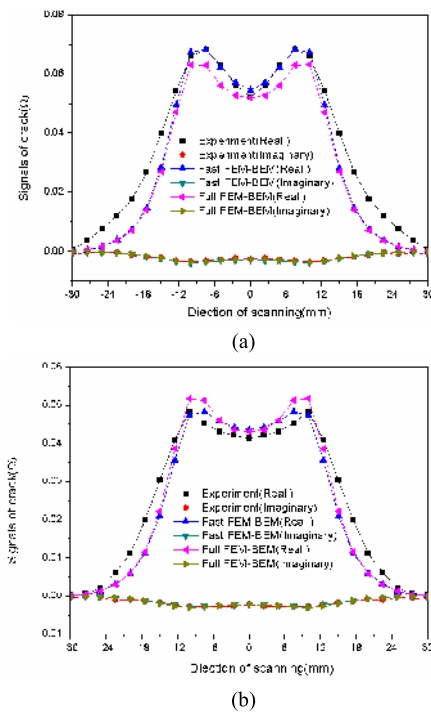| Coil | Inner diameter(mm) | 6.0 |
	Outer diameter (mm)	7.0
	Height (mm)	10.0
	Number of turns	44
Test condition	Exciting current(A)	1.0
	Lift-off(mm)	1.0
	Frequency(MHz)	3.0

(a)

(b)

FIGURE 10. Comparison of experimental results and simulated results. (a) Crack C1. (b) Crack C2.

test-piece. The probe is scanned 60 mm along the crack length with a pitch of 2.5 mm.

C. EXPERIMENTAL RESULTS AND COMPARISON WITH NUMERICAL SIMULATIONS

The measured ECT signals due to the crack C1 and C2 in the CFRP plate with comparison with the numerical results are given in Figure 10. The difference signals between the

detection and the reference coils are illustrated. At the same time, 25 signals at the position around the each scanning point are averaged to reduce noise. as it is not possible to control the exact amplitude of the driving current in this experimental system, calibrations are conducted on the measured signals to make them comparable with the numerical results. First the calibration coefficients are obtained through making the experimental results and simulation results of crack C1 the same (as shown in Fig. 10(a)). Then these calibration coefficients are used to transform the other measured signals.

Figure 10 shows the calibrated experimental signals and the simulated signals using the developed fast solver and the full FEM-BEM code for 2 slit cracks in the CFRP laminate plate, where the "Experiment", "Full FEM-BEM" and "Fast FEM-BEM" denote the calibrated experimental signals, the signals calculated with the full FEM-BEM code and the results obtained by using the new fast forward simulator, respectively. The real and imaginary ECT signals at the different scanning points are given in the both figures. All the signals show good agreement with each other, and the two simulation results are almost fully identical, which reveals that the new fast forward simulation code can give satisfactory simulation accuracy for ECT of laminated CFRP material. The good agreement between the experimental results and the simulation demonstrated the validity of the proposed ECT fast forward solver for the CFRP anisotropic material. At the same time, the new fast solver required only less than 10 seconds for the results given in Fig.10, which is much less than the 50 minutes of the full FEM-BEM code.

V. CONCLUSION

In this paper, a novel fast forward solver for ECT signal simulation of CFRP anisotropic material is developed and validated. First, a numerical simulation model of CFRP laminate plate is proposed. Second, a new rapid forward simulation scheme based on a database strategy is established for the efficient simulation ECT of CFRP material, and is implemented on the basis of an FEM-BEM code. Finally, an ECT measurement system is built for experimental validation of the new fast forward solver. Comparisons with the numerical results simulated by using the full FEM-BEM code and the experimental results demonstrated that the proposed new fast forward scheme can predict ECT signals for CFRP material with high precision and over 300 times faster than the conventional FEM-BEM method.

REFERENCES

[1] E. Kirkby, R. de Oliveira, V. Michaud, and J. A. Månson, "Impact localisation with FBG for a self-healing carbon fibre composite structure," *Compos. Struct.*, vol. 94, no. 1, pp. 8–14, 2011.

[2] M. Z. Sadeghia, P. Nienheysen, S. Arslan, A. Dafnis, B. S. Marció, R. H. Schmitt, and K. U. Schröder, "Damage detection by double-sided ultrasonic assessment in low-velocity impacted CFRP plates," *Compos. Struct.*, vol. 208, pp. 646–655, Jan. 2019.

[3] S. E. Burrows, A. Rashed, D. P. Almond, and S. Dixon, "Combined laser spot imaging thermography and ultrasonic measurements for crack detection," *Nondestruct. Test. Eval.*, vol. 22, nos. 2–3, pp. 217–227, Feb. 2007.

[4] V. Munoz, B. Valés, M. Perrin, M. L. Pastor, H. Welemane, A. Cantarel, and M. Karama, "Damage detection in CFRP by coupling acoustic emission and infrared thermography," *Compos. B, Eng.*, vol. 85, pp. 68–75, Feb. 2016.

[5] W. L. Lai, S. C. Kou, C. S. Poon, W. F. Tsang, and C. C. Lai, "Characterization of the deterioration of externally bonded CFRP-concrete composites using quantitative infrared thermography," *Cement Concrete Compos.*, vol. 32, no. 9, pp. 740–746, 2010.

[6] S. Senck, M. Scheerer, V. Revol, B. Plank, C. Hannesschläger, C. Gusenbauer, and J. Kastner, "Microcrack characterization in loaded CFRP laminates using quantitative two- and three-dimensional X-ray dark-field imaging," *Compos. A, Appl. Sci. Manuf.*, vol. 115, pp. 206–214, Dec. 2018.

[7] C. Goidescu, H. Welemane, C. Garnier, M. Fazzini, R. Brault, E. Péronnet, and S. Mistou, "Damage investigation in CFRP composites using full-field measurement techniques: Combination of digital image stereo-correlation, infrared thermography and X-ray tomography," *Compos. B, Eng.*, vol. 48, pp. 95–105, May 2013.

[8] M. Ueda, K. Mimura, and T.-K. Jeong, "*In situ* observation of kink-band formation in a unidirectional carbon fiber reinforced plastic by X-ray computed tomography imaging," *Adv. Compos. Mater.*, vol. 25, no. 1, pp. 31–43, 2016.

[9] A. Ghoshal, W. N. Martin, M. J. Schulz, A. Chattopadhyay, W. H. Prosser, and H. S. Kim, "Health monitoring of composite plates using acoustic wave propagation, continuous sensors and wavelet analysis," *J. Reinf. Plast. Compos.*, vol. 26, no. 1, pp. 95–112, 2007.

[10] M. Giordano, A. Calabro, C. Esposito, A. D'Amore, and L. Nicolais, "An acoustic-emission characterization of the failure modes in polymer-composite materials," *Compos. Sci. Technol.*, vol. 58, no. 12, pp. 1923–1928, 1998.

[11] W. Yin, P. J. Withers, U. Sharma, and A. J. Peyton, "Non-contact characterisation of carbon-fibre-reinforced plastics (CFRP) using multi-frequency eddy current sensors," in *Proc. IMTC*, Warsaw, Poland, May 2007, pp. 1–4.

[12] K. Mizukami, Y. Mizutani, A. Todoroki, and Y. Suzuki, "Detection of in-plane and out-of-plane fiber waviness in unidirectional carbon fiber reinforced composites using eddy current testing," *Compos. B, Eng.*, vol. 86, pp. 84–94, Feb. 2016.

[13] M. A. Machado, K.-N. Antin, L. S. Rosado, P. Vilaça, and T. G. Santos, "Contactless high-speed eddy current inspection of unidirectional carbon fiber reinforced polymer," *Compos. B, Eng.*, vol. 168, pp. 226–235, Jul. 2019.

[14] J. Cheng, J. Qiu, H. Ji, E. Wang, T. Takagi, and T. Uchimoto, "Application of low frequency ECT method in noncontact detection and visualization of CFRP material," *Compos. B, Eng.*, vol. 110, pp. 141–152, Feb. 2017.

[15] G. Bardl, A. Nocke, C. Cherif, M. Pooch, M. Schulze, H. Heuer, M. Schiller, R. Kupke, and M. Klein, "Automated detection of yarn orientation in 3D-draped carbon fiber fabrics and preforms from eddy current data," *Compos. B, Eng.*, vol. 96, pp. 312–324, Jul. 2016.

[16] Y. Du, S. Xie, Z. Chen, G. Zhu, and P. Li, "Detectability evaluation of eddy current testing probes for inspection of defects in carbon fiber reinforced polymer laminates," *Int. J. Appl. Electromagn. Mech.*, vol. 55, no. 2, pp. 185–193, 2017.

[17] M. Berger, B. Egloff, M. Summa, M. Schwarz, G. Lanza, and H.-G. Herrmann, "Conception of an eddy current in-process quality control for the production of carbon fibre reinforced components in the RTM process chain," *Procedia CIRP*, vol. 62, pp. 39–44, Jan. 2017.

[18] H. Kosukegawa, Y. Kiso, Y. Yoshikawa, R. Urayama, and T. Takagi, "Characterization of laminated structure on scarfed slope of CFRP by utilizing eddy current testing with differential type probe," *Int. J. Appl. Electromagn. Mech.*, vol. 59, no. 4, pp. 1227–1238, 2019.

[19] H. Heuer, M. Schulze, M. Pooch, S. Gäbler, A. Nocke, G. Bardl, C. Cherif, M. Klein, R. Kupke, R. Vetter, F. Lenz, M. Kliem, C. Bülow, J. Goyvaerts, T. Mayer, and S. Petrenz, "Review on quality assurance along the CFRP value chain—Non-destructive testing of fabrics, preforms and CFRP by HF radio wave techniques," *Compos. B, Eng.*, vol. 77, pp. 494–501, Aug. 2015.

[20] K. Mizukami, Y. Mizutani, A. Todoroki, and Y. Suzuki, "Analytical solutions to eddy current in carbon fiber-reinforced composites induced by line current," *Adv. Compos. Mater.*, vol. 25, no. 4, pp. 385–401, 2016.

[21] Z. Chen, K. Miya, and M. Kurokawa, "Rapid prediction of eddy current testing signals using A-ϕ method and database," *NDT&E Int.*, vol. 32, no. 1, pp. 29–36, Jan. 1999.

[22] Z. Chen, N. Yusa, and K. Miya, "Sizing of volumetric stress corrosion crack from eddy current testing signals with consideration of crack width," *Stud. Appl. Electromagn. Mech.*, vol. 28, pp. 259–266, 2007.

[23] S. Xie, B. Fang, W. Cai, M. Tian, H.-E. Chen, and Z. Chen, "Sizing of defects in special shaped coolant pipe of Tokamak magnet based on eddy current testing signals," *Int. J. Appl. Electromagn. Mech.*, vol. 52, nos. 1–2, pp. 307–314, 2016.

[24] L. Wang and Z. Chen, "Reconstruction of stress corrosion cracks using high-dimension hybrid optimization algorithm from eddy current signals," *Int. J. Appl. Electromagn. Mech.*, vol. 52, nos. 3–4, pp. 1511–1517, 2016.

[25] S. Xie, M. Tian, P. Xiao, C. Pei, Z. Chen, and T. Takagi, "A hybrid nondestructive testing method of pulsed eddy current testing and electromagnetic acoustic transducer techniques for simultaneous surface and volumetric defects inspection," *NDT&E Int.*, vol. 86, pp. 153–163, Mar. 2017.

[26] Z. Chen, N. Yusa, M. Rebican, and K. Miya, "Inversion techniques for eddy current NDE using optimization strategies and a rapid 3D forward simulator," *Int. J. Appl. Electromagn. Mech.*, vol. 20, nos. 3–4, pp. 179–187, 2004.

[27] S. Xie, Z. Chen, T. Takagi, and T. Uchimoto, "Development of a very fast simulator for pulsed eddy current testing signals of local wall thinning," *NDT&E Int.*, vol. 51, pp. 45–50, Oct. 2012.

[28] S. Xie, Z. Chen, H.-E. Chen, X. Wang, T. Takagi, and T. Uchimoto, "Sizing of wall thinning defects using pulsed eddy current testing signals based on a hybrid inverse analysis method," *IEEE Trans. Magn.*, vol. 49, no. 5, pp. 1653–1656, May 2013.

[29] Z. Chen, N. Yusa, and K. Miya, "Some advances in numerical analysis techniques for quantitative electromagnetic nondestructive evaluation," *Nondestruct. Test. Eval.*, vol. 24, nos. 1–2, pp. 69–102, Mar. 2009.

[30] S. Xie, L. Wu, Z. Tong, H.-E. Chen, Z. Chen, T. Uchimoto, and T. Takagi, "Influence of plastic deformation and fatigue damage on electromagnetic properties of 304 austenitic stainless steel," *IEEE Trans. Magn.*, vol. 54, no. 8, Aug. 2018, Art. no. 6201710.

[31] M. Fan, B. Cao, A. I. Sunny, W. Li, G. Tian, and B. Ye, "Pulsed eddy current thickness measurement using phase features immune to liftoff effect," *NDT&E Int.*, vol. 86, no. 3, pp. 123–131, 2017.

[32] A. Todoroki, M. Tanaka, and Y. Shimamura, "Measurement of orthotropic electric conductance of CFRP laminates and analysis of the effect on delamination monitoring with an electric resistance change method," *Compos. Sci. Tech.*, vol. 62, no. 5, pp. 619–628, 2002.

[33] M. Weber and M. R. Kamal, "Estimation of the volume resistivity of electrically conductive composites," *Polym. Compos.*, vol. 18, no. 6, pp. 711–725, 1997.

[34] H. Menana and M. Féliachi, "3-D eddy current computation in carbon-fiber reinforced composites," *IEEE Trans. Magn.*, vol. 45, no. 3, pp. 1008–1011, Mar. 2009.

[35] J. Cheng, H. Ji, J. Qiu, T. Takagi, T. Uchimoto, and N. Hu, "Novel electromagnetic modeling approach of carbon fiber-reinforced polymer laminate for calculation of eddy currents and eddy current testing signals," *J. Compos. Mater.*, vol. 49, no. 5, pp. 617–631, 2015.

YALI DU received the B.S. and M.S. degrees from the Physics Department, Northwest University, Xi'an, China, in 2002 and 2008, respectively. She is currently pursuing the Ph.D. degree with the School of Aerospace Engineering, Xi'an Jiaotong University, Xi'an.

Since 2007, she has also been a Lecturer with the School of Science, Xi'an Polytechnic University, Xi'an, China. Her research interests include theory and application of electromagnetic nondestructive evaluation, and inverse problems in non-destructive testing.

SHEJUAN XIE received the B.S. and M.S. degrees from Xi'an Jiaotong University, Xi'an, China, in 2006 and 2009, respectively, and the Ph.D. degree from the Institute of Fluid Science, Tohoku University, Sendai, Japan, in 2012, where she was a Postdoctoral Fellow, from 2012 to 2013.

Since 2013, she has been an Associate Professor with the School of Aerospace Engineering, Xi'an Jiaotong University. She has authored of two books and more than 80 articles. She holds more than 20 patents. Her research interests include implementation and application of electromagnetic and ultrasonic nondestructive testing, inspection and maintenance technology for nuclear engineering, and the design and optimization of the probe.

TETSUYA UCHIMOTO received the B.S. and M.S. degrees in nuclear engineering and the Ph.D. degree in engineering from The University of Tokyo, Tokyo, Japan, in 1993, 1995, and 1998, respectively.

He is currently a Professor with the Institute of Fluid Science, Tohoku University, Sendai, Japan. He has authored three books and more than 300 articles. His research interests include evaluation of degradation of structural materials by electromagnetic nondestructive evaluation, such as austenitic stainless steels, nickel based alloys and high Cr ferritic steels, material characterization of cast irons by eddy-current testing, and novel sensor development.

XUDONG LI received the B.S. degree from Xi'an Jiaotong University, Xi'an, China, in 2016. He is currently pursuing the Ph.D. degree with the School of Aerospace Engineering, Xi'an Jiaotong University, Xi'an.

His research interests include numerical simulation of the three-dimensional eddy current problem and magneto-mechanical coupled problem.

ZHENMAO CHEN received the B.Sc. and M.Eng. degrees from Xi'an Jiaotong University, Xi'an, China, in 1984 and 1987, respectively, and the D.Eng. in nuclear engineering from The University of Tokyo, Tokyo, Japan, in 1998.

He was an Assistant Professor with Xi'an Jiaotong University, from 1987 to 1994. He was also a Lecturer and an Associate Professor with Keio University, from 2002 to 2005. In 2005, he became a Professor with the School of Aerospace, Xi'an Jiaotong University, Xi'an. He has authored six books and more than 500 articles. He holds more than 40 patents. His current research interests include electromagnetic nondestructive evaluation, applied electromagnetics and mechanics, and fusion engineering.

TOSHIYUKI TAKAGI received the B.Eng., M.Eng., and D.Eng. degrees in nuclear engineering from The University of Tokyo, Tokyo, Japan, in 1977, 1979, and 1982, respectively.

From 1982 to 1987, he was a Researcher with the Energy Research Laboratory, Hitachi Ltd., and an Associate Professor with The University of Tokyo, from 1987 to 1989. From 1989 to 1998, he was an Associate Professor with the Institute of Fluid Science, Tohoku University, Sendai, Japan, where he has been a Professor, since 1998. He has authored more than 20 books and 500 articles. His current research interests include electromagnetic nondestructive evaluation, diamond and diamond-like carbon coatings and their application, and adaptive structural systems using shape memory alloy.

• • •